Body-Earth Mover's Distance: A Matching-Based Approach for Sleep Posture Recognition

Xiaowei Xu, *Student Member, IEEE*, Feng Lin, *Member, IEEE*, Aosen Wang, *Student Member, IEEE*, Yu Hu, *Member, IEEE*, Ming-Chun Huang, *Member, IEEE*, and Wenyao Xu, *Member, IEEE*

Abstract—Sleep posture is a key component in sleep quality assessment and pressure ulcer prevention. Currently, body pressure analysis has been a popular method for sleep posture recognition. In this paper, a matching-based approach, Body-Earth Mover's Distance (BEMD), for sleep posture recognition is proposed. BEMD treats pressure images as weighted 2D shapes, and combines EMD and Euclidean distance for similarity measure. Compared with existing work, sleep posture recognition is achieved with posture similarity rather than multiple features for specific postures. A pilot study is performed with 14 persons for six different postures. The experimental results show that the proposed BEMD can achieve 91.21% accuracy, which outperforms the previous method with an improvement of 8.01%.

Index Terms—Earth Mover's Distance, pressure image, shape descriptor, sleep posture analysis.

I. INTRODUCTION

SLEEP posture has been proven to be a key component in sleep quality assessment and pressure ulcer prevention. As a critical indicator for sleep quality, sleep posture has been widely studied for medical diagnoses and sleep disease treatment [1]–[3], and is a promising method to provide more insight into sleep quality assessment. Furthermore, sleep posture plays an important role in pressure ulcer prevention. Pressure ulcers are one of the main problems for post-surgical patients and elderly patients. To date, more than 2.5 million people in the United States suffer from pressure ulcers every year [4]. However, there is no long-term monitoring for sleep posture to ensure that the pressure is distributed in a proper way. Therefore, there is an urgent need for autonomously monitoring sleep postures for medical diagnoses and pressure ulcer prevention.

In the last decade, several approaches to monitor sleep posture autonomously have been proposed. Cameras including video cameras [5], [6] and near-infrared cameras [7] have been used to recognize sleep postures. However, this approach suffers from privacy concerns and image noise due to low visibility at night. Another approach [8] adopted inertial sensors, including accelerometers, gyroscopes, and magnetometers. These sensors have to be attached to human bodies, which is inconvenient for patients during sleep.

Recently, the approach of dispersed pressure sensors which are embedded in the mattress has become promising [9]–[11]. The sensor-embedded mattress can record the pressure distribution of human bodies, which forms a pressure image. Compared with other solutions (i.e., wearable sensors and cameras), this sensing modality is unobtrusive to users and minimizes privacy concerns. Prior work in this approach focused on detecting posture changes rather than recognizing sleep postures [12]–[15]. Recently, Liu *et al.* [16] adopted 32 features of pressure images for classification of *six* sleep postures. Ostadabbas *et al.* [17] made the classification with 13 features of pressure images for *three* sleep postures. In this approach, features are posture-specific, and it is difficult to obtain a universal feature set for different gesture recognition applications. For example, feature *Symmetry* (measure of pressure symmetry) is for prone recognition, and feature *ShArea* (area in pixels of bounding box of shoulder) is sensitive to identifying supine postures [16]. Therefore, these methods for sleep posture recognition are based on local features and individualized pre-training, which requires considerable effort to apply in a large population.

Considering the characterization of the pressure array, pressure images can be regarded as weighted 2D projected shapes (pressure images) of 3-D subjects (human bodies). A popular approach for 2D shape classification is to convert the 2D shapes to histograms with descriptors [18]. Recently, Earth Mover's Distance (EMD) has been proven to be a robust metric for histogram matching, which has been widely applied in a series of applications [19]–[21]. Unlike Euclidean distance, EMD can avoid quantization and other binning problems in similarity computing between histograms [22]. Thus, EMD has the potential to be a promising method for sleep posture recognition with pressure images.

In this paper, an application-specific distance metric, Body-Earth Mover's Distance (BEMD), for sleep posture recognition is proposed. The contribution of the paper is three-fold: 1) A matching-based approach, BEMD, with no local features for sleep posture recognition is proposed; 2) BEMD treats pressure images as weighted 2D shapes with shape descriptors, and combines EMD and Euclidean distance for matching with region segmentations. A skew-based sleep posture classifier is proposed for sleep posture classification with matching results;

3) Compared with previous work, accuracy is significantly improvement by 8.01%. The improvement of accuracy and runtime of 4-region segmentation over the original space can be as large as 46.92% and 18.28x, respectively.

The rest of the paper is organized as follows. In Section II, a brief background of EMD and ground distance is introduced. The overall design of the Smart Bedsheet system is presented in Section III. Section IV presents the proposed approach, including pre-processing, BEMD, and skew-based sleep posture classifier. The experiments and conclusions are given in Sections V and VI, respectively.

II. BACKGROUND AND PRELIMINARIES

A. Earth Mover's Distance

EMD is derived from a transportation problem, which has been proven to be a robust distance metric for image retrieval in the year 2000 [23]. EMD is a m-to-n matching formulation, which is a more generalized similarity metric than 1-to-1 matching (e.g., Euclidean distance) and 1-to-n matching (e.g., Hausdorff distance). In the last decade, EMD has been applied to many applications, such as contour matching [21], document similarity search [24], 3D object retrieval [25], and hand gesture recognition [19].

EMD is used to calculate the similarity between signatures, which are compact representations of distributions. A signature with N clusters is defined as a set $S = \{(s_i, k_i), 1 \leq i \leq N\}$, where s_i is the position of the ith cluster, k_i is its weight, and N is the size of the signature. There are two signatures, $A = \{(a_i, \alpha_i), 1 \leq i \leq n\}$ and $B = \{(b_j, \beta_j), 1 \leq j \leq m\}$ with m and n clusters, respectively. The cost set, cost $= \{c_{ij}, 1 \leq i \leq n, 1 \leq j \leq m\}$ are given, where c_{ij} is the ground distance between clusters a_i and b_j. EMD is used to find a flow, $F = \{f_{ij}, 1 \leq i \leq n, 1 \leq j \leq m\}$, that minimizes the overall cost

$$\text{EMD}(A, B) = \min \left\{ \sum_{i=1}^{n} \sum_{j=1}^{m} c_{ij} f_{ij} \right\} \quad (1)$$

subject to the following constraints:

$$f_{ij} \geq 0, 1 \leq i \leq n, 1 \leq j \leq m \quad (2)$$

$$\sum_{i=1}^{n} \alpha_i = \sum_{j=1}^{m} \beta_j \quad (3)$$

$$\sum_{j=1}^{m} f_{ij} = \alpha_i, \quad 1 \leq i \leq n \quad (4)$$

$$\sum_{i=1}^{n} f_{ij} = \beta_j, \quad 1 \leq j \leq m. \quad (5)$$

Usually, the feature space where a_i and b_j live is also called space. The design of ground distance is involved with space, which will be discussed in detail in the next subsection. EMD has a high time complexity of $O(n^3 \log n)$. It should be highlighted that EMD can be modeled as a transportation problem, in which the object is to transport the good, "weight," from suppliers, "a_i," to consumers, "b_j" with minimal cost. An illustration of EMD with A and B is presented in Fig. 1. Usually, more clusters, more discrete weight sets and cost sets
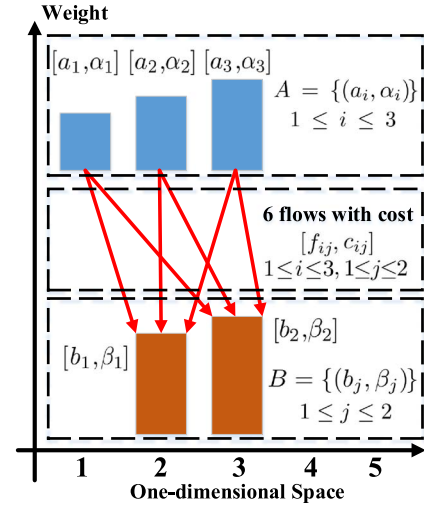

Fig. 1. Illustration of Earth Mover's Distance. Signature A and B have three and two clusters, respectively. There are potentially 6 flows that transport weight from clusters of A to clusters of B. Each flow has a cost indicating the cost per unit of weight. In the one-dimension space, the cost (or the ground distance) can be defined as linear distance, e.g., $c_{11} = c(a_1, b_1) = |1 - 2| = 1$, and $c_{12} = c(a_1, b_2) = |1 - 3| = 2$. Other ground distances can also be adopted. There exits multiple solutions (a set of flows with transported weights) that can fulfill the transportation with different overall costs, and EMD is the one with the minimal overall cost.
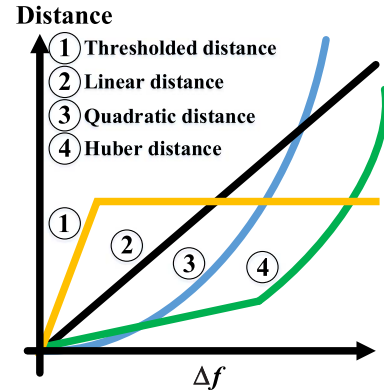

Fig. 2. Illustration of the four popular ground distances used in this paper: thresholded distance, linear distance, quadratic distance and Huber distance.

will make the minimal solution more complex, which results in a longer computing time. For example, there are two cost sets, $\text{cost}_1 = \{1, 4, 9, 16\}$ and $\text{cost}_2 = \{1, 2, 3, 4\}$. cost_1 is more complex than cost_2, because by selecting two cost values, the situations that $1+2=3$ and $1+3=4$ exist in cost_1 and do not in cost_2. This situation is the same by selecting more cost values. Thus, the potential number of cost values of cost_2 is larger than that of cost_1, which will take more time for EMD computing. Weight sets have the same character with cost set, and more details can be found in [23].

B. Ground Distance

Ground distance determines the distance between two clusters or features in the defined space. Ground distance is also known as penalty function in convex optimization [26]. As shown in Fig. 2, four popular penalty functions, linear distance, quadratic distance, Huber loss distance, and thresholded distance, are introduced.
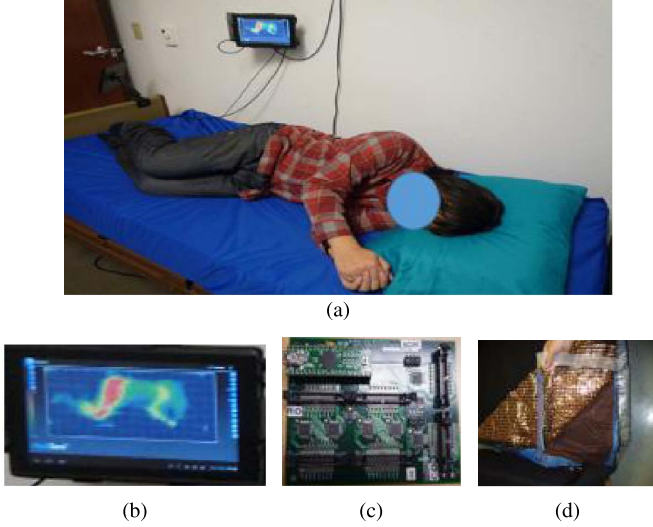
Fig. 3. (a) The Smart Bedsheet system in use and its submodules. (b) Terminal (a tablet). (c) Scanning module. (d) E-textile with conductive lines.

Linear distance (or l_1-norm) is widely used in image retrieval applications [23]. It increases relatively slowly with the difference of two features, which is defined as

$$D_{\text{linear}} (f_1, f_2) = a \times \Delta f_{12} \qquad (6)$$

where a is the gradient of the line, and f_1 and f_2 are two features defined in the space.

Quadratic distance (or l_2-norm) is also used in image retrieval and image classification [27]. It increases much faster than linear distance, which is defined in Formula (7). b is a weighted factor, and the definition of f_1 and f_2 is the same for formula (6)

$$D_{\text{quadratic}} (f_1, f_2) = b \times \Delta f_{12}^2. \qquad (7)$$

Huber distance [28] is linear for values smaller than thr, and quadratic for larger values. Thus, it has different characterizations in each of its pieces, and it gives the same sensitivity to outliers as the quadratic distance, and the same low penalty to neighbors as linear distance. Huber loss distance is defined as follows:

$$D_{\text{Huber}} (f_1, f_2) = \begin{cases} a \times \Delta f_{12}, & \text{if } \Delta f_{12} \leq \text{thr} \\ b \times \Delta f_{12}^2, & \text{otherwise.} \end{cases} \qquad (8)$$

Thresholded distance assesses a fixed distance to residuals larger than the threshold, thr. Thus it is relatively insensitive to outliers. Thresholded distance is defined as

$$D_{\text{threshold}} (f_1, f_2) = \begin{cases} c \times \Delta f_{12}, & \text{if } \Delta f_{12} \leq \text{thr} \\ d, & \text{otherwise} \end{cases} \qquad (9)$$

where thr is the threshold, and d is the fixed distance. Thresholded distance has been used by Pele *et al.* [27] for approximated EMD calculations.

III. THE SMART BEDSHEET SYSTEM

The prototype of the Smart Bedsheet system [29] is shown in Fig. 3. The system consists of three components: a 64×128 pressure sensor array, a data sampling unit, and a terminal for data analysis and storage. Multiple devices can be selected as
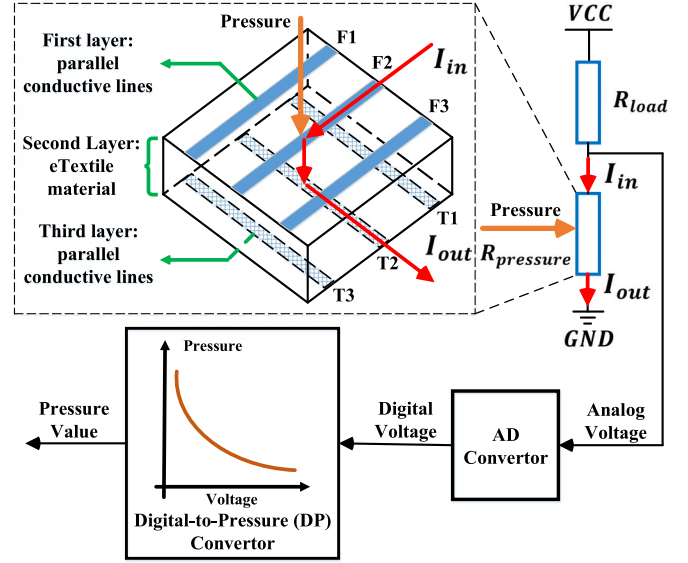

Fig. 4. Illustrations of the Smart Bedsheet system with a 3×3 pressure sensor array: each of the first and third layer has three conductive lines and are orthogonal. The middle layer contains eTextile material, which is pressure-sensitive.

the terminal, and a tablet is chosen for the system. In order to achieve high resolution, comfort and low cost, piezo-electrical pressure sensors are selected for the sensor array, which has three layers as shown in Fig. 3(d). The first layer is normal fabric uniformly coated with 64 parallel conductive lines. The middle layer is the eTextile material [30]. The bottom is with 128 parallel conductive lines (perpendicular to the top 64 lines). The data sampling unit [as shown in Fig. 3(c)] scans all the vertical and horizontal lines to produce a resistance map of the entire bedsheet. The terminal [a tablet as shown in Fig. 3(b)] converts the resistance map to 8-bit digital values to create a pressure image. The Universal Serial Bus (USB) interface is adopted to connect the data sampling unit and the terminal.

As shown in Fig. 5, the pressure transmission flow is presented in detail with a 3×3 pressure sensor array. When there is pressure detected in the area, as shown in Fig. 5, the pressure change will be captured by scanning all mental lines. At some time, the conduct lines, $F2$ of the first layer and $T2$ of the third layer are selected. Then, the current will flow through the intersection area (full of eTextile material) of the two conductive lines. By selecting different combinations of the conductive lines (totally 9 combinations) in the first and the third layers, I_{in} and I_{out} will also change, and all intersections will be searched. The eTextile material of each intersection works as a pressure sensitive resistor, R_{pressure}. R_{load} is a resistor with a fixed value. The two resistors are connected in series, thus the voltage drop of each resistance is proportional to its resistance value. Therefore, the pressure is firstly translated into resistance. Then, further translation to voltage drop is performed. The voltage drop is measured with an analog-to-digital (AD) convertor. With a pre-measured relational table of pressure and voltage drop, the real pressure can be easily produced with the voltage drop in the digital-to-pressure (DP) module. By scanning all combinations of the conductive lines (totally 9 combinations) in the first and the third layer, one pressure image is obtained. With a proper sampling rate, dynamic pressure images are produced.
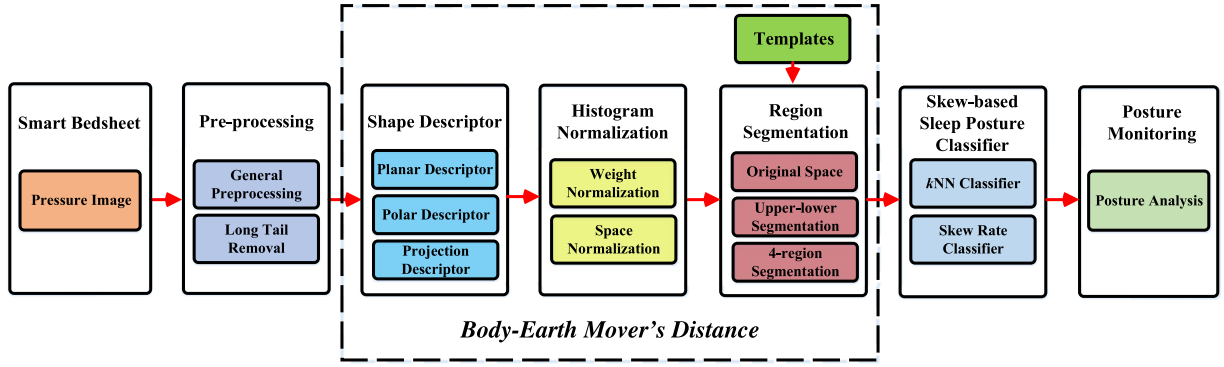
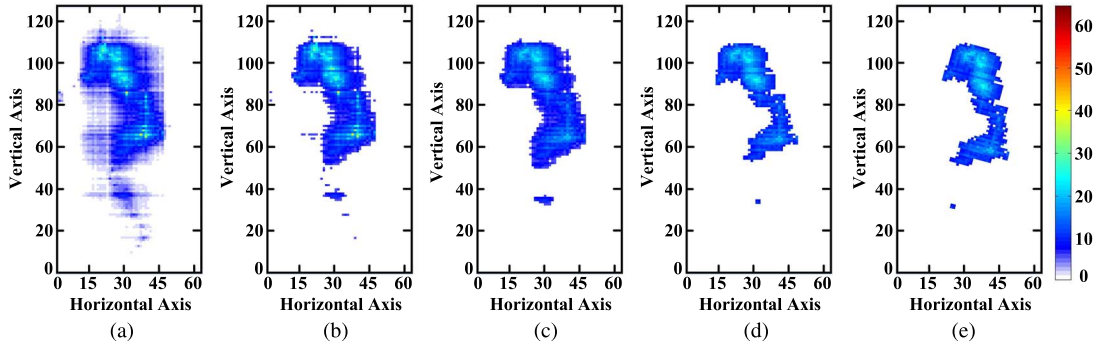Fig. 5. The sleep posture recognition framework.

Fig. 6. Four steps in pressure image preprocessing. (This picture should be seen in color.) (a) Original pressure image. (b) Threshold pressure image. (c) Gaussian-filtered pressure image. (d) Long-tail-removed pressure image. (e) Rotated pressure image.

IV. THE MATCHING-BASED APPROACH

The sleep posture recognition framework with BEMD is shown in Fig. 5. Raw pressure images are captured by the Smart Bedsheet system. With BEMD, the similarity between two pressure images are obtained, which will be classified by the skew-based sleep posture classifier. The classification results are further analyzed to monitor the sleep posture. Pre-processing, BEMD and the skew-based sleep posture classifier are discussed in detail in this section.

A. Pre-Processing

Pre-processing of the pressure image is to remove the offset of position and orientation on the bedsheet. In pre-processing, four steps are adopted as shown in Fig. 6. Threshold filtering, Gaussian filtering and rotation are general pre-processing methods [17]. Long tail removal is specific for pressure images with the elastic eTextile material.

1) Threshold Filtering: At the beginning, the pressure image is filtered with a threshold. Suppose the pressure of each point in the pressure image is $p_{i,j}$, $1 \leq i \leq 128$, $1 \leq j \leq 64$. The threshold is set to

$$\text{PreThr} = \frac{\sum_{i=1}^{n} \sum_{j=1}^{m} p_{ij}}{N} \qquad (10)$$

where N is the number of non-zero pressure points. The pressure point with a value smaller than the threshold is assigned to zero

$$p_{i,j} = \begin{cases} p_{i,j}, & \text{if } p_{i,j} \leq \text{PreThr} \\ 0, & \text{otherwise.} \end{cases} \qquad (11)$$
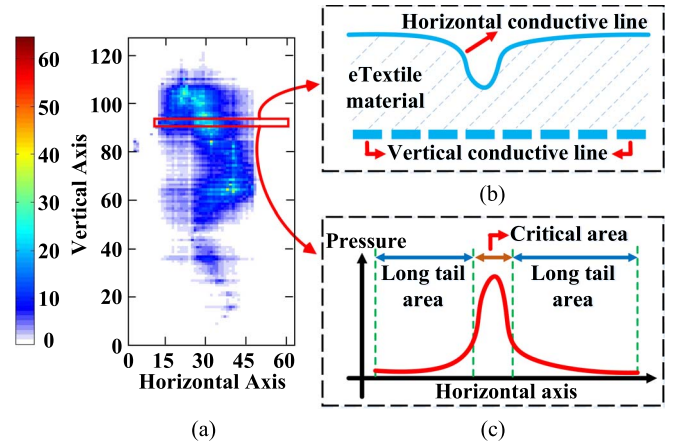

Fig. 7. Illustration of the long tail pressure in the pressure sensor array. (a) A horizontal conductive line is selected in a pressure image with left fetus posture. (b) The deformation of the eTextile material between the selected horizontal conductive line and all vertical conductive lines. (c) The pressure distribution of the selected horizontal conductive line, and the critical area and long tail area of the pressure distribution. (It should be noted that there are 64 vertical conductive lines in the bedsheet system, and only 8 are presented in (b) for compact explanation).

2) Gaussian Filtering: Secondly, a low-pass Gaussian filter of a symmetric 5×5 unit is applied to remove noises.

3) Long Tail Removal: The third step is to remove the long tail area of pressure areas. The long tail area of the pressure image is a characterization of eTextile material as shown in Fig. 7. As illustrated in Fig. 7(c), the critical area is defined as the small area that directly make contacts with the pressure areas, and the long tail area is the area which is derived by the
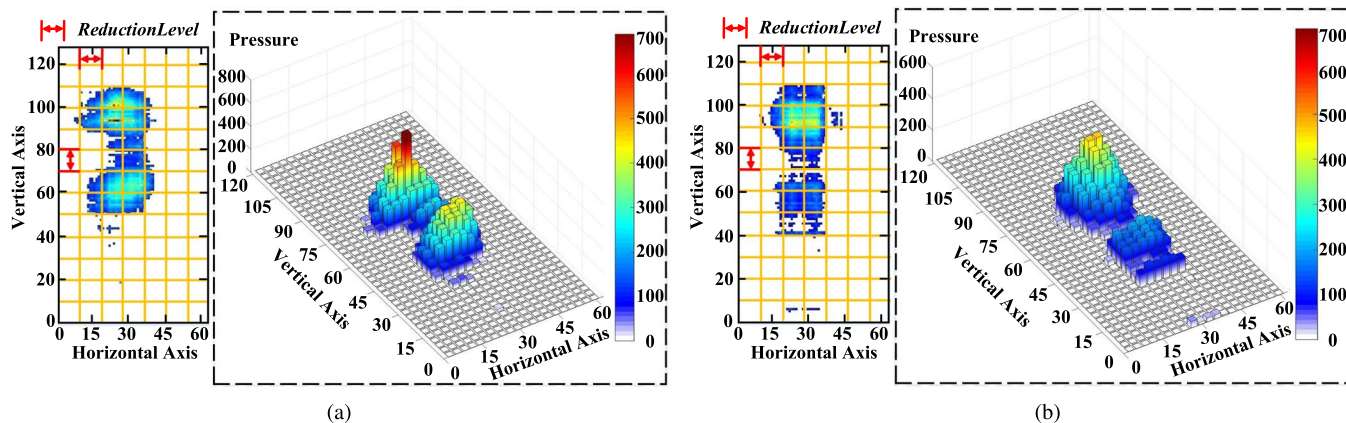
Fig. 8. Histograms with planar descriptor of (a) left fetus and (b) supine (ReductionLevel = 3). The pressure image are divided with grids, and the pressure images are described with bins in a plane. The ReductionLevel is the side length of the grid, which determines the resolution of the planar histograms for pressure images. It should be noted that the number of grids in the pressure image is much less than the number to produce the planar histograms in both (a) and (b), which is for clear explantation. The figures should be seen in color to have a better visualization.
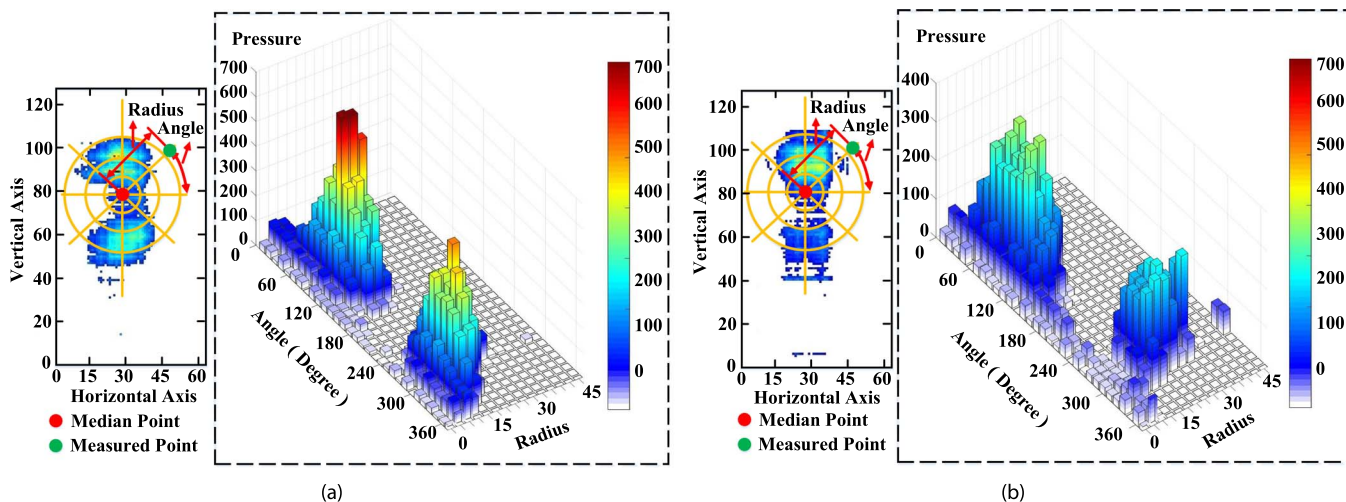

Fig. 9. Histograms with polar descriptor of (a) left fetus and (b) supine. The pressure image are divided by circles and their radiuses, in which every region (arc strips) corresponds to one bin in the histograms in both (a) and (b). Thus, the pressure image is described as a histogram in a plane. A measured point is introduced to show the pressure to calculate the angle and the radius of some point. It should be noted that the number of arc strips in the pressure image is much less than the number to produce the polar histograms in both (a) and (b), which is for clear explantation. The figures should be seen in color to have a better visualization.

critical areas around it. The long tail removal is adopted to clear the information redundancy in pressure images. Two benefits are achieved in this step: 1) the negative influence of the long tail area to EMD calculation is eliminated; 2) the description of pressure images becomes compact, which can simplify EMD calculations. As shown in Fig. 6(d), the pressure area is much smaller than that in Fig. 6(c).

4) Rotation: The last step adopts principal component analysis (PCA) to rotate the pressure image. The rotation angle is equal to the angle between the leading eigenvector of the PCA result and the long edge of the pressure image.

B. Body-Earth Mover's Distance

In this subsection, BEMD first formulates the sleep posture recognition problem with shape descriptors. Then, histogram normalization is applied for meaningful BEMD computing. At last, BEMD is applied with segmentation which combines EMD and Euclidean distance for similarity measure. Median point which is defined as the center of mass considering the pressure

of each point is frequently used in this subsection. It should be noted that the histogram is a special type of signatures, and each bin of histograms corresponds to a cluster in the signature.

1) Problem Formulation With Shape Descriptors: In order to evaluate the similarity of pressure images with BEMD, pressure images need to be transformed into histograms, and the definition of space, cost, and weight in EMD is then introduced. Three shape descriptors are adopted for histogram production in BEMD: planar descriptor, polar descriptor and projection descriptor as shown in Figs. 8–10, respectively. The planar descriptor is a relatively straightforward method for two-dimension (2D) pressure images. The polar descriptor is also known as angular radial transform [31], which is a popular region-based descriptor. The projection descriptor is derived from projection-based lower bounds for EMD [22], which adopts projected histograms (that live in a lower dimension compared with the original histogram) to calculate the lower bound of the original histograms. In this paper, the projected one-dimension (1D) histograms for two-dimension (2D) pressure images are regarded as descriptors.
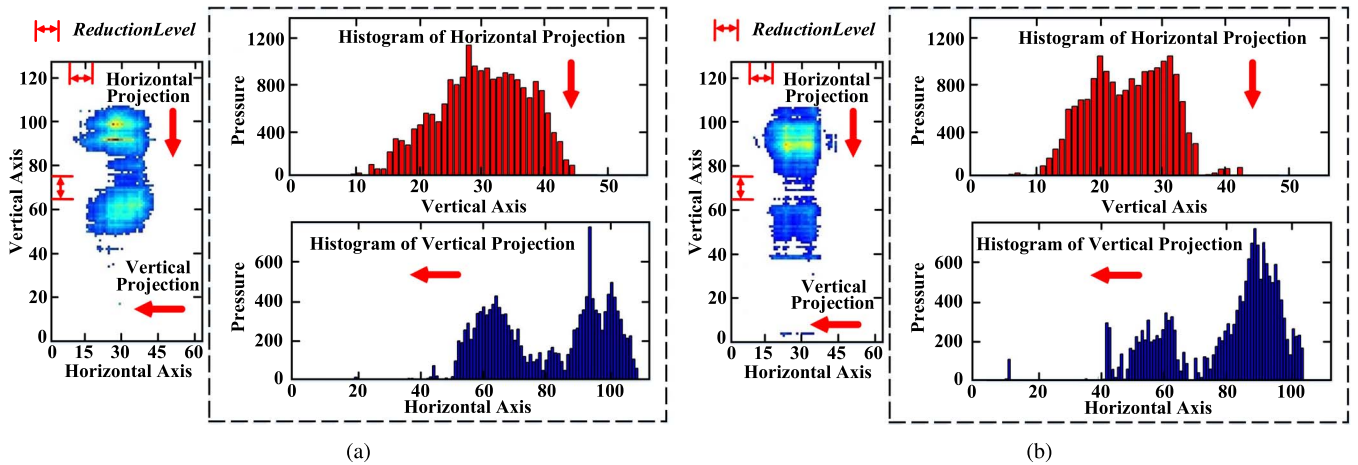
Fig. 10. Horizontal and vertical histograms with projection descriptor of (a) left fetus and (b) supine (ReductionLevel = 3). The pressure image are projected to horizontal and vertical directions, and the pressure image is described with histograms in a line. It should be noted that the number of grids in the pressure image is much less than the number to produce the projection histograms in both (a) and (b), which is for clear explantation.

Planar Descriptor: The planar descriptor puts pressure images into a plane with grids as shown in Fig. 8. The pressure of each grid is the pressure sum of the points that fall into it. The side length of each grid, reductionLevel, determines the resolution of the descriptor, and a small reductionLevel value leads to a high-resolution description. The highest resolution of the planar descriptor is the resolution of the bedsheet system. The x and y axis of the plane are the horizontal and vertical axis of the bedsheet, respectively. The z axis is the pressure sum of each grid. As EMD has a high time complexity of $O(n^3 \log n)$, reductionLevel should be set to a proper value considering resolution and processing time.

With the planar descriptor and reductionLevel, the pressure image is compressed as shown in Fig. 8. The bin distributions can effectively present the pressure distributions of the pressure images, and the difference between different sleep postures are remarkable. For the left fetus posture, the pressure of the shoulder and hip are both high, and it is highly asymmetric in the horizontal axis. Compared with the left fetus posture, the supine posture has a big difference between the pressures of shoulders and hips, and the bin distribution in the horizontal axis is almost symmetric.

Polar Descriptor: The polar descriptor puts the pressure image into a polar plane with arc strips as shown in Fig. 9. The pressure of each arc strip is the pressure sum of the points that fall into it. With the median point as the center, multiple circles and radius are selected and determine the resolution of the descriptor. The x and y axis of the plane represent the angle and radius, respectively. The z axis is the pressure sum of each arc strip. It should be noted that 0 and 360 degrees are equal in the angle axis; that is to say, two points with angles of 30 and 330 degrees have the same distance to the point with 0 degree when these points have the same radius. With the same consideration of the high time complexity of EMD, the number of circles and radius should not be too large.

With the polar descriptor, the pressure image is compressed as shown in Fig. 9. The bin distributions have a small distortion with original pressure images. The part with angle from 0 degree to 180 degrees corresponds to the pressure points that

have a bigger vertical value than the median point, or the upper part of the body (mainly the shoulders). While the part with an angle from 180 to 360 degrees corresponds to the pressure points that have a smaller vertical value than the median point, or the lower part of the body (mainly the hips and legs). The polar descriptor is very similar to the planar descriptor, and the only difference is the resolution. The resolution varies with different radiuses for the polar descriptor, while the resolution of the planar descriptor is uniform for the whole space.

Projection Descriptor: The projection descriptor projects the pressure points to horizontal and vertical directions. As shown in Fig. 10, the pressure images of supine and left fetus postures are projected to horizontal and vertical directions. Thus two histograms are created for the two directions. The axis x of the histogram corresponds to the horizontal/vertical axis of the bedsheet, and the axis y corresponds to the pressure sum of the pressure points that have the same vertical/horizontal axis on the bedsheet.

With projection, the information of pressure images in 2D space is condensed to 1D histograms. Though some information is lost due to projection, the difference between the supine posture and the left fetus posture is still obvious as shown in Fig. 10. For horizontal projection of the left fetus posture, there is only one peak in the histogram. While for the supine posture with horizontal projection, the histogram has two peaks. This is due to the fact that the left and right shoulder both bear a large fraction of the total pressure in the supine posture. For vertical projection of the left fetus posture, the main two pressure peaks corresponding to the shoulder and the hip have similar total pressures. However, for the supine posture with vertical projection, the pressure sum of the two main pressure peaks has a significant difference. This may be caused by the fact that shoulder bears more pressure in the supine posture than that in the left fetus posture.

Space, Cost, and Weight Formulation: With histograms produced by histogram descriptors, the space, cost, and weight in BEMD can be defined. For histograms produced by the projection descriptor and the planar descriptor, space is the horizontal and vertical axis of the bedsheet. While for histograms

produced by the polar descriptor, space is composed of angle and radius. Thus, space of polar descriptor and planar descriptor is a 2D Euclidean space, while space of projection descriptor is a 1D Euclidean space. Defining the ground distance of cost in Euclidean space has been introduced in Section II-B. The weight is the pressure, which needs to be transported from one histogram to another. For example, suppose the pressure is 36 in point $(35, 78)$ and ReductionLevel $= 1$ for the planar descriptor. Then, a new bin is introduced in the histogram of the planar descriptor with $a_i = (35, 78)$ and $\alpha_i = 36$. The formulation for polar and projection descriptors are the same with the planar descriptor.

2) Histogram Normalization: This part is to normalize space and weight for meaningful BEMD calculations. For pressure images, weight normalization and space alignment are required to remove the offset of weight, position, and size for different subjects. In the weight normalization, the pressure value of each pressure point is divided by the sum of all pressure points first. Then, each pressure value is multiplied by a predefined weight, or the standard weight (in this paper, the standard weight is the average weight of all subjects). Thus, all subjects have the same normalized weight.

The space alignment has two steps: origin normalization and scaling normalization. The origin normalization is used to tackle the different sleep positions on the bedsheet, which is achieved by updating coordinates minus the vertical and horizontal values of the median points. Thus, the median points become origins of the space for all pressure images. Body Mass Index (BMI) is adopted for scaling normalization, which is defined as weight divided by height squared with weight measured in kilograms and height measured in meters [32]. BMI is assumed to be the same value to reduce the influence of body sizes. Based on this assumption, the scaling factor f_s, is defined as follows:

$$f_s = \left(\frac{W_n}{W}\right)^{\frac{1}{2}} \tag{12}$$

where W_n is the standard weight (in this paper, the average weight is selected as the standard weight). For planar and projection descriptors, the value in the vertical/horizontal axis is updated by multiplying by f_s. For the polar descriptor, only the value in the radius axis need to be updated by multiplying by f_s.

Compared with Fig. 11(a), the weight of each pressure point in Fig. 11(b) increases as the subject's weight is below the standard weight. Thus, the scaling factor is larger than one, and the pressure area in Fig. 11(b) is much larger than that in Fig. 11(a). It should be noted that the origin is also changed to the median point of the new pressure image.

3) Region Segmentation: In order to achieve speedup, the region segmentation is proposed in BEMD to avoid unpractical or insignificant flows. Thus, BEMD is a combination of EMD and Euclidean distance. For EMD, matching is unlimited, which means that each bin of one histogram has the potential to match any bin in another histogram. While for Euclidean distance, matching is strictly limited, and each bin of one histogram can only be matched to the bin with the same feature (or coordinate) in another histogram. BEMD with segmentation has two levels:
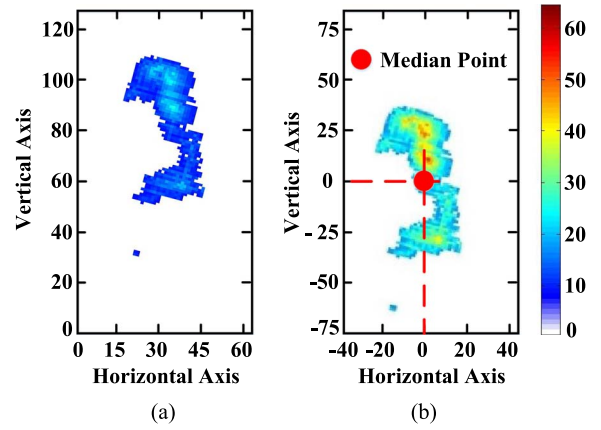

Fig. 11. Histogram normalization for pressure images. (a) Without histogram normalization. (b) With histogram normalization. For clarity of presentation, pressure images are used here to describe the effect of histogram normalization.

Euclidean level and EMD level. In Euclidean level, the space is divided into m regions

$$\text{space} = \sum_{i=1}^{m} \text{sub}_i \tag{13}$$

where sub_i is a subspace of the space. In EMD level, EMD is calculated for each subspace. BEMD is the weighted sum of the EMD for each subspace as shown below

$$\text{BEMD}(A, B) = \sum_{i=1}^{n} \varepsilon_i \, \text{EMD}(A_i, B_i) \tag{14}$$

$$A_i, B_i \subseteq \text{sub}_i \tag{15}$$

where ε_i is a weight factor and sub_i is the subspace. A_i and B_i are the subsets of A and B, respectively. Both A_i and B_i live in subspace sub_i. Therefore, BEMD can be regarded as Euclidean distance when just considering subspaces, which are matched to the corresponding subspaces. For the similarity of corresponding subspaces, EMD is performed. The implementation of space segmentation is up to specific applications.

For sleep posture recognition with pressure images, two space segmentations are implemented: upper-lower segmentation and 4-region segmentation as shown in Fig. 12. Two benefits are achieved by space segmentation. Firstly, unpractical flows are avoided. As shown in Fig. 12(a), the interference between the upper and lower part of the body is removed by upper-lower segmentation. Furthermore, the dissimilarity introduced by left-right asymmetry of sleep postures can be better measured with left-right segmentation in 4-region segmentation. Further segmentation is not applied as there exists variances for sleep postures, especially for left and right fetus postures.

C. Skew-Based Sleep Posture Classifier

The skew-based sleep posture classifier has two stages, kNN classifier and skew rate classifier, as shown in Algorithm 1. Suppose the training template contains sleep postures of m subjects, and there are totally p sleep postures considered. A skew rate $s_i \, (1 \leq i \leq p)$, is assigned to each sleep posture,
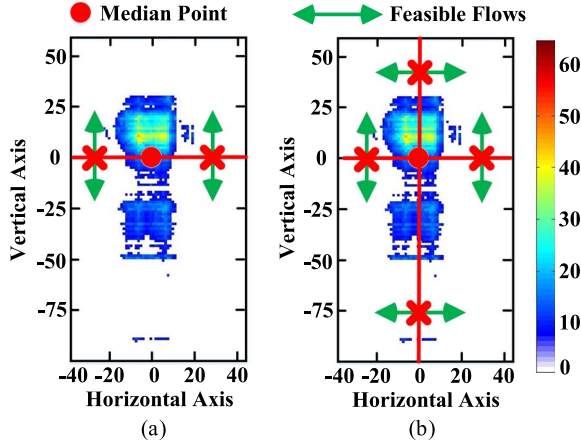
Fig. 12. Two region segmentations with median point as the segmenting point. (a) Upper-lower segmentation. (b) 4-region segmentation. By segmentation, the feasible flows between the segmented regions are cancelled.
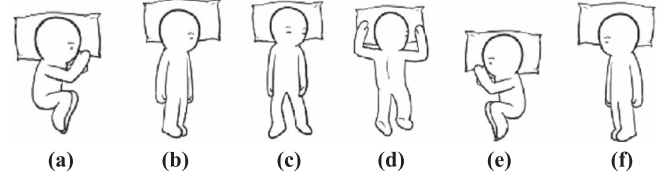

Fig. 13. Six sleep postures considered in the experiment. (a) Right fetus. (b) Right log. (c) Supine. (d) Prone. (e) Left fetus. (f) Left log.

TABLE I
EXPERIMENT SETUP

Module	Parameter
Linear Distance	$a=1$
Quadratic distance	$b=1$
Huber distance	$a=1$, $b=1$, $thr=20$
Thresholded distance	$c=1$, $d=thr$, $thr=20$
Planar Descriptor	$ReductionLevel=3$
Polar Descriptor	$AngleNum=36$, $RadiusLevel=5$
Projection Descriptor	$ReductionLevel=1$
Region segmentation of BEMD	$\varepsilon_i = 1, 1 \leqslant i \leqslant m$

which indicates the inclining degree of the sleep posture. For example, as prone and supine postures have a symmetry pressure distribution on the horizontal directions, the skew rates are set to zero. For the log posture, there is a slight difference of the pressures on the left and right part of the body, and their skew rates are assigned to one. Compared with the log posture, the fetus posture is more symmetric because their arms and legs are twisted. Thus, a larger skew rate should be allocated. The sign of the skew rates represent the direction of the postures.

Algorithm 1 Skew-based Sleep Posture Classifier

Input: template$[m]$, test;
Output: testClass;
 1: // **Stage One**: kNN **Classifier**;
 2: **for** $i = 1 \to m$ **do**
 3:     oneVote = $\boldsymbol{k}$NN(template$[i]$, test);
 4:     vote[oneVote] $\leftarrow$ vote[oneVote] $+ 1$;
 5: **end for**
 6: // **Stage Two: Skew Rate Classifier**;
 7: Obtain maxVote and maxCate by exploring vote$[i]$;
 8: **if** maxVote $\geqslant m/2$ **then**
 9:     testClass = maxCate;
10: **else**
11:     testSkew = $(\sum_{i=1}^{m}$ skew$_i \times$ vote$_i)/N$;
12:     testClass = $\boldsymbol{k}$NN(testSkew, skew$_i$);
13: **end if**
14: return testClass;

Stage one is to apply kNN for each subject in the templates. Then, each subject has its vote oneVote, indicating which category of sleep postures the test sample should be. vote$[p]$ is created by combining all oneVote. In stage two, the highest vote maxVote, with its category maxCate, is produced by exploring vote$[p]$. If maxVote is equal to or larger than $m/2$, the class of the test sample is maxCate. Otherwise, the median skew rate of the test sample is calculated as shown in Line 11 of Algorithm 1. The test sample is assigned to the posture whose skew rate is nearest to the median skew rate.

V. EXPERIMENTS

A. Experiment Setup

There were 14 subjects in the experiment, which includes nine males and five females. The weight of the subjects ranged from 55 to 85 kilograms, and the height was between 155 and 185 centimeters. The bedsheet system was deployed on a standard twin-size coil spring mattress during the experiment. As shown in Fig. 13, six postures including Left-Log (LL), Left-Fetus (LF), Right-Log (RL), Right-Fetus (RF), Prone (P) and Supine (S) were investigated, which is the same with the previous study [29]. The skew rates of the six postures, LL, LF, RL, RF, P, and S are -1, -2, $+1$, $+2$, 0, 0, respectively. In data collection, 22 samples were recorded for each of the six postures for each subject. Thus there are 132 samples for each subject. Variations in body, arm and leg positions were allowed, and the system was tested on a range of positions that fall within the six postures.

Leave One Out Cross Validation (LOOCV) was used to test the proposed approach. In the experiment, one subject's data was selected as the test data, and the rest was regarded as the training data. This process was repeated for each person. For ground distances, descriptors and BEMD, the parameters were configured as shown in Table I. Considering the high time complexity of $O(n^3 \log n)$ for EMD, ReductionLevel, AngleNum, and RadiusLevel were set to a proper value so that the computing time per sample would not exceed five minutes (too longer computing time leads to too much delay, which can not provide enough samples for monitoring and meaningful analysis).

The average number of bins for each sample of the three descriptors with different space segmentation is shown in Table II. It should be noted that the average number of bins for the planar descriptor and the polar descriptor has an about 50% reduction by applying upper-lower segmentation. The same situation also exists in upper-lower segmentation and 4-region segmentation with the planar descriptor and the polar descriptor. However, the projection descriptor shows a very different trend. This is due to

TABLE II
AVERAGE NUMBER OF BINS FOR EACH HISTOGRAM

Histogram Descriptor	Original Space	Upper-lower Segmentation	4-region Segmentation
Planar Descriptor	132.91	66.46	33.23
Polar Descriptor	169.56	84.78	42.39
Projection Descriptor	42.72	27.35	19.57

TABLE III
OVERALL ACCURACY AND RUNTIME

Descriptor	Accuracy	Runtime Per Sample (Seconds)
Planar	90.26%	8.07
Polar	89.26%	15.96
Projection	91.21%	3.27

TABLE IV
COMPARISON WITH THE PREVIOUS WORK

Approach	# of Features	# of postures	Accuracy	Improvement
[29]	32	6	**83.20%**	N/A
This work	0	6	**91.21%**	**8.01%**

the fact that space segmentation has a very different influence on the 1D projection. For example, there is one histogram of v bins in the vertical direction and another one histogram of h bins in the horizontal direction in the origin space. With upper-lower segmentation, there are two histograms of about $v/2$ bins in the vertical direction and two histograms of both about h bins in the horizontal direction. All the experiments are run with Matlab R2013a on a standard desk computer with 8 GB RAM and an Intel i7-3770 CPU.

B. Performance

In this subsection, the overall performance is presented. Detailed comparison of each posture is also introduced. Comparison with the previous work [29] is discussed.

1) Overall Accuracy and Runtime: The configuration of the overall performance is as follows: 1) the widely-used linear distance in image retrieval is adopted; 2) 4-region segmentation is used to eliminate unpractical flows for high accuracy. As shown in Table III, the overall accuracy and runtime are presented. There is no significant difference between the three descriptors for accuracy. However, for runtime, there is a clear gap. The runtime of the polar descriptor doubles that of the planar descriptor, which also doubles the runtime of the projection descriptor. Projection descriptor consumes much less time while it achieves the highest accuracy.

A comparison with the previous work is shown in Table IV. The proposed BEMD has an accuracy improvement of 8.01% compared with [29]. The main advantage of BEMD is that it is matching-based rather than feature-based.

2) Accuracy of Each Posture: The detailed precision and recall results of the overall accuracy with the three descriptors are shown in Tables V–VII. The f-measure accuracies of the planar descriptor, the polar descriptor and the projection descriptor are 90.26%, 89.26%, and 91.21%, respectively. For the reader's convenience, the confusion matrix of the previous work [29] is presented in Table VIII. When considering precision and recall, the accuracy of the log posture is relatively lower than the other

TABLE V
POSTURE CLASSIFICATION CONFUSION MATRIX (%)
WITH **PLANAR** DESCRIPTOR

	LL	LF	P	RL	RF	S	Recall
LL	86.16	1.73	0.35	3.46	0	8.30	**86.16**
LF	2.21	97.79	0.00	0	0	0	97.79
P	0.39	1.95	94.94	1.56	0	1.17	94.94
RL	4.36	0	0.29	89.83	0.58	4.94	89.83
RF	0	0	3.80	8.70	87.50	0.00	87.50
S	3.44	0	0.38	11.83	0.38	83.97	83.97
Precision	89.23	96.38	95.17	**77.86**	98.91	**85.35**	**90.26**

TABLE VI
POSTURE CLASSIFICATION CONFUSION MATRIX (%)
WITH **POLAR** DESCRIPTOR

	LL	LF	P	RL	RF	S	Recall
LL	84.08	2.08	0	1.04	0	12.80	**84.08**
LF	3.54	94.69	1.33	0	0	0.44	94.69
P	0.39	2.34	95.70	0.39	0	1.17	95.70
RL	5.54	0	0.58	83.97	0.58	9.33	**83.97**
RF	0.00	0	3.80	6.52	89.13	0.54	89.13
S	3.82	0	0.38	7.63	1.15	87.02	87.02
Precision	86.35	95.54	94.01	**84.35**	98.10	**78.18**	**89.26**

TABLE VII
POSTURE CLASSIFICATION CONFUSION MATRIX (%)
WITH **PROJECTION** DESCRIPTOR

	LL	LF	P	RL	RF	S	Recall
LL	88.58	1.38	0.69	4.50	0	4.84	88.58
LF	2.65	95.58	1.33	0	0	0.44	95.58
P	0.78	3.11	93.77	0.78	0	1.56	93.77
RL	2.33	0.58	0.58	92.44	0	4.07	92.44
RF	0.00	1.09	1.63	2.72	89.67	0.54	89.67
S	3.82	0.38	0.38	9.54	0	83.21	**83.21**
Precision	90.24	93.59	95.31	**84.06**	100.00	87.90	**91.21**

TABLE VIII
POSTURE CLASSIFICATION CONFUSION MATRIX (%)
OF THE **PREVIOUS WORK** [29]

	LL	LF	P	RL	RF	S	Recall
LL	70.63	2.80	1.75	6.29	1.75	16.78	**70.63**
LF	0.70	88.11	6.29	1.75	2.10	1.05	88.11
P	0.35	7.69	87.06	0.35	3.50	1.05	87.06
RL	4.20	9.79	0.70	78.67	3.50	3.15	**78.67**
RF	0.00	3.85	5.24	1.75	89.86	0.70	89.86
S	9.44	3.15	1.05	0.35	1.05	84.97	84.97
Pricision	82.79	**76.36**	85.27	88.24	88.32	**78.90**	**83.20**

postures for all three descriptors. As there is a great variance for arm and leg in the log posture, its projection histograms for BEMD have a high possibility to be different from each other, but to be similar with that of other postures. For the fetus posture, it has a very asymmetric pressure distribution (the pressure is mainly distributed on the left/right part of the body for the right/left fetus posture), then it can be recognized with a high accuracy. For the prone posture, it has a symmetric pressure distribution, including two arms, and its pressure distributions in the vertical projection histograms are different from each other. Thus, its accuracy can be relatively high. However, for the supine posture, the symmetric pressure is mainly distributed on the shoulder and hip, which is very similar with the log posture. Thus, its accuracy is relatively low. The accuracy of the polar
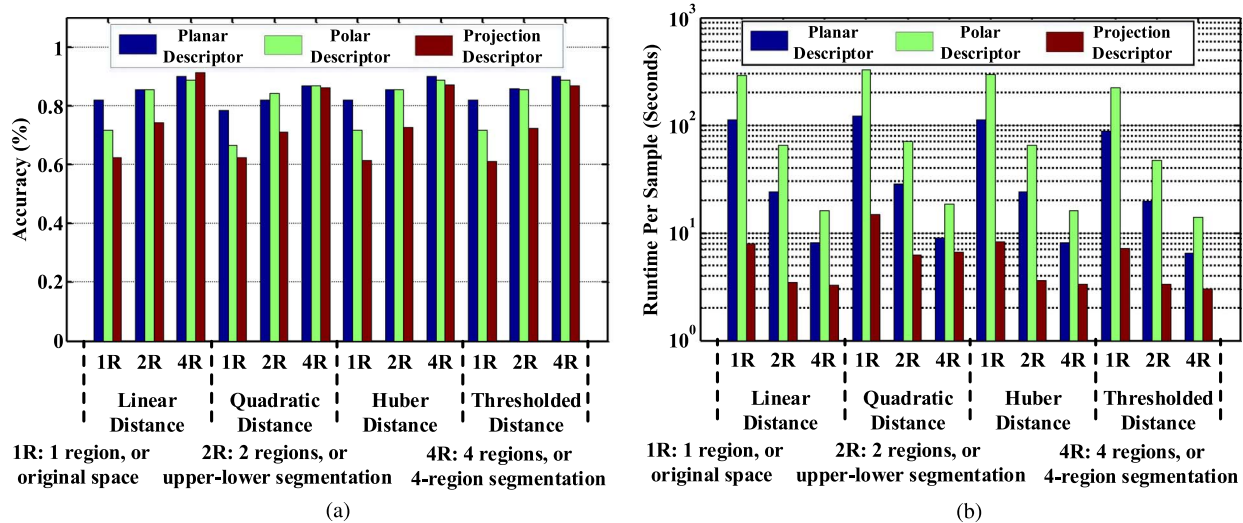
Fig. 14. The sensitivity of (a) accuracy and (b) runtime to descriptor with different configurations.

descriptor for the supine posture is relatively higher than that of the other two descriptors. This is due to the fact that the polar descriptor has a relatively higher resolution on the hip and shoulder areas. The histograms with higher resolutions can better extract the symmetric feature of the supine posture.

Compared with the confusion matrix of the previous work [29], the proposed results of the the three descriptors have higher accuracies for almost all postures. This is because the feature-based approach depends on local features which are relatively more sensitive to noises than the matching-based approach. The improvement of left log, prone and supine postures are markable. This is caused by three factors: 1) Histograms derived from global descriptors can better describe the symmetry character of supine and prone postures; 2) In the matching approach, all postures from all templates are taken into consideration, which is more robust; 3) Skew rate is used for indistinctness postures, which also takes the skew rates of all postures into consideration.

C. Sensitivity Analysis

1) Sensitivity to Descriptor: As shown in Fig. 14(a) and (b), the sensitivity of accuracy and runtime to descriptor with different configurations is presented. In the original space, the planar descriptor achieves the highest accuracy. The polar descriptor has a relatively low accuracy, which is due to its characterization. The polar descriptor describes the area around the median point with a high resolution, which is not a critical area for sleep posture classification. Therefore, although with more bins, the polar descriptor has a relatively low accuracy. The projection descriptor gets the lowest accuracy, which is due to the fact that it has a relatively larger information loss for describing the 2D image with 1D projection descriptors.

With region segmentation, the gap of accuracies between different descriptors is reduced, and the accuracies of the three descriptors have no significant difference with 4-region segmentation. Compared with other descriptors, the projection descriptor has a relatively larger improvement. This is caused by the fact that with space segmentation, 2D pressure images get a

high resolution for the projection descriptor. Planar and polar descriptors are 2D descriptors, which have a better description of 2D pressure images than the 1D descriptor, projection descriptor. Thus, the accuracy of planar and polar descriptors in the original space is much higher than that of the projection descriptor. Space segmentation divides the space into several subspaces, and the projection descriptor can get projected histograms in each of the subspaces. Therefore, the posture information in 2D pressure images can be better extracted with the projection descriptor and space segmentation.

The runtime of the three descriptors is proportional to their number of bins. Polar descriptor has the highest number of bins, thus, its runtime is the largest.

2) Sensitivity to Ground Distance: As shown in Fig. 15(a) and (b), the sensitivity of accuracy and runtime to ground distance with different configurations is presented. As linear distance and square distance are both belong to the l_x-norm distance metric, the accuracies and runtime are almost the same for the two distances. The runtime of quadratic distance is relatively larger than that of linear distance. This is because square distance has a more discrete cost set, which makes the mapped transportation network more complex. As Huber distance is a combination of linear distance and square distance, its accuracy and runtime are between that of linear distance and quadratic distance. Thresholded distance ignores the outliers and assigns the same distance when the distance is larger than thr, which simplifies the cost set and also introduces some errors. It can be learned that if the thr is large enough, the accuracy and runtime are almost the same with that of linear distance. Therefore, its accuracy is almost the same with linear distance as thr is relatively large.

There is no significant difference among the linear distance, quadratic distance and Huber distance for runtime. Compared with other ground distances, the runtime of thresholded distance has a speedup of 1.04x–2.24x. This is because that thresholded distance assigns the distance a consistent value if it is larger than thr, thus the mapped transportation network is simplified.

3) Sensitivity to Region Segmentation: As shown in Fig. 16(a) and (b), the sensitivity of accuracy and runtime to
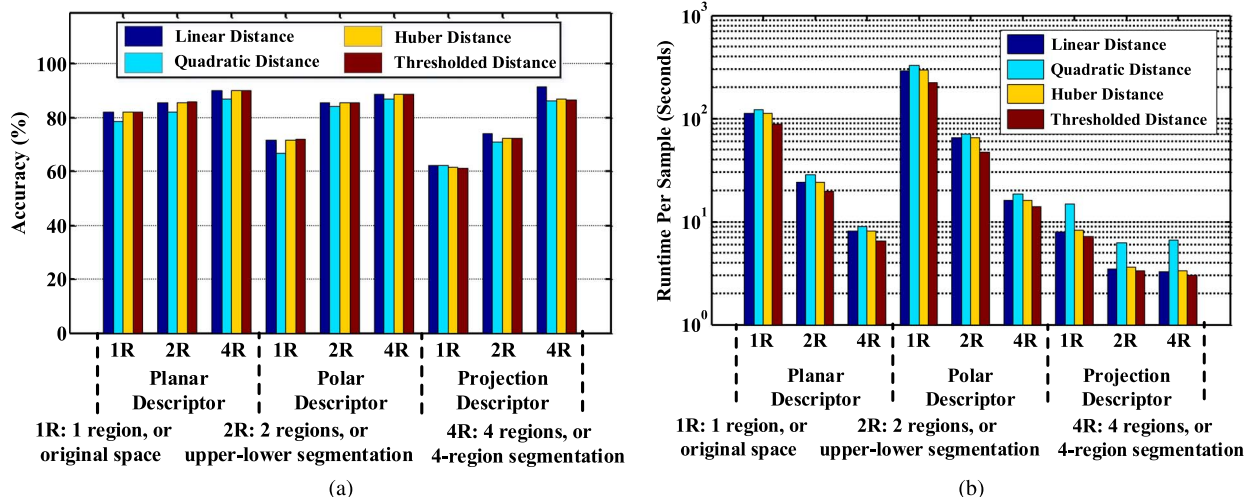
Fig. 15. The sensitivity of (a) accuracy and (b) runtime to ground distance with different configurations.
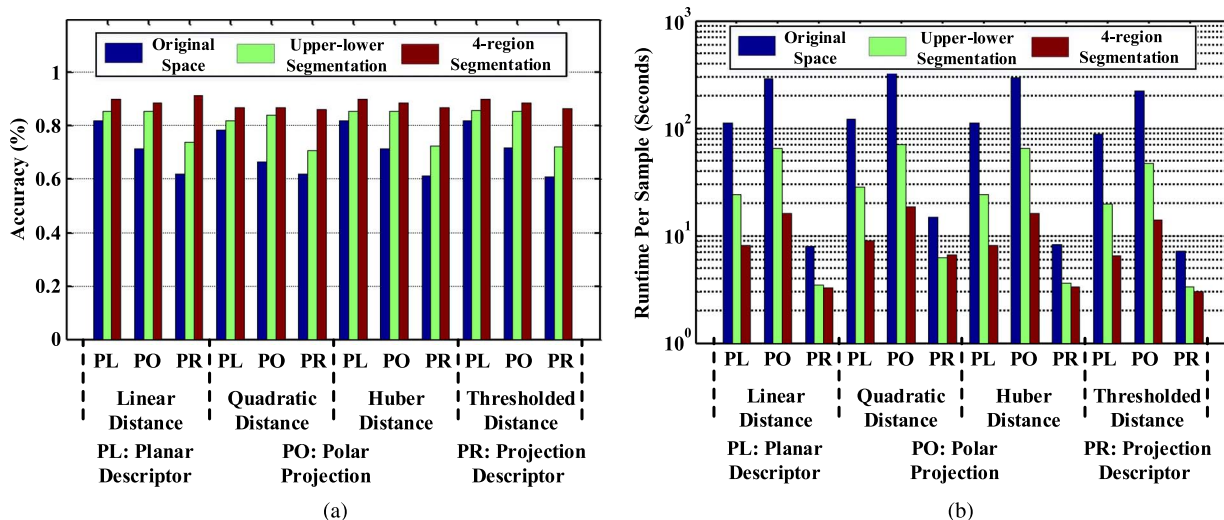

Fig. 16. The sensitivity of (a) accuracy and (b) runtime to region segmentation to descriptors with different configurations.

region segmentation with different configurations is presented. When the number of subspaces increases, the accuracies of all three descriptors also increase. The largest accuracy improvement is achieved by the projection descriptor. Compared with the original space, the accuracy of the projection descriptor with 4-region segmentation has an improvement of 46.92%. This is caused by the fact that space segmentation can better extract information and remove unpractical flows.

Furthermore, there is a large speedup of runtime with the increasing number of segmented subspaces. A rough mathematic analysis is made here for explanation. The upper-lower segmentation divides the origin space into two subspaces, and the time complexity of the worst case is $2 \times (n/2)^3 \log(n/2)$. Thus compared with the original space in the worst case, the speedup is about $[1 \times (n)^3 \log(n)]/[2 \times (n/2)^3 \log(n/2)] = 4 \times \log(n)/\log(n/2) > 4$. The computing time is also influenced by the weight and cost sets, or the complexity of the mapped transportation network. Thus, the speedup varies with different descriptors and space segmentations. For 2D descriptors, the speedup of the origin space over 4-segmentation (13.46x∼18.28x) is higher than that (2.24x∼2.47x) of the 1D

descriptor, the projection descriptor. This is caused by two facts. Firstly, 2D descriptors have a more complex cost set than 1D descriptors, e.g., using linear distance, one bin can have four nearest neighbors with a distance of one, while there are only two for bins in 1D space. With space segmentation, the more complex cost gets a larger simplification. Secondly, the number of bins in planar and polar descriptors are larger than that of the projection descriptor, which also has a more complex mapped transportation network. With space segmentation, more complexity reduction is achieved with planar and polar descriptors than the projection descriptor.

VI. CONCLUSION

In this paper, a matching-based approach, BEMD is presented for sleep posture recognition with a pressure sensitive bedsheet. BEMD firstly converts pressure distributions into histograms with three descriptors. Then histogram normalization is applied with body mass index (BMI). At last, BEMD combines EMD and Euclidean distance to evaluate the similarity of sleep postures. Specific methods in pre-processing and classification are

also proposed. Long tail removing is presented to removal information redundancy, and a skew-based sleep posture classifier is proposed for classification. Compared with existing work, no local feature extraction is involved. Comprehensive experiments are conducted, and four widely used ground distances-linear distance, square distance, Huber distance and thresholded distance-are tested. The achieved accuracy of 91.21% outperforms the previous work with an improvement of 8.01%. Compared with original space, the improvement of accuracy and runtime of 4-region segmentation can be as large as 46.92% and 18.28x, respectively. In future work, applying the approach to clinical sleep applications such as sleep stage recognition [33] will be the focus. BEMD will be combined with other time-series metrics for dynamic sleep posture recognition, which can be regarded as a 4D metric that considers space and time domains.

REFERENCES

[1] J. Jin and E. Sanchez-Sinencio, "A home sleep apnea screening device with time-domain signal processing and autonomous scoring capability," *IEEE Trans. Biomed. Circuits Syst.*, vol. 9, no. 1, pp. 96–104, 2015.

[2] C. Ambrogio, X. Lowman, M. Kuo, J. Malo, A. R. Prasad, and S. Parthasarathy, "Sleep and non-invasive ventilation in patients with chronic respiratory insufficiency," *Intensive Care Med.*, vol. 35, no. 2, pp. 306–313, 2009.

[3] A. Oksenberg and D. S. Silverberg, "The effect of body posture on sleep-related breathing disorders: Facts and therapeutic implications," *Sleep Med. Rev.*, vol. 2, no. 3, pp. 139–162, 1998.

[4] L. Soban, S. Hempel, B. Ewing, J. N. Miles, and L. V. Rubenstein, "Preventing pressure ulcers in hospitals," *Joint Commis. J. Quality Patient Safety*, vol. 37, no. 6, pp. 245–252, 2011.

[5] K. Nakajima, Y. Matsumoto, and T. Tamura, "A monitor for posture changes and respiration in bed using real time image sequence analysis," in *Proc. IEEE 22nd Annu. Int. Conf. IEEE Eng. Med. Biol. Soc.*, 2000, vol. 1, pp. 51–54.

[6] Y.-T. Peng, C.-Y. Lin, M.-T. Sun, and C. A. Landis, "Multimodality sensor system for long-term sleep quality monitoring," *IEEE Trans. Biomed. Circuits Syst.*, vol. 1, no. 3, pp. 217–227, 2007.

[7] W.-H. Liao and C.-M. Yang, "Video-based activity and movement pattern analysis in overnight sleep studies," in *Proc. IEEE19th Int. Conf. Pattern Recognit.*, 2008, pp. 1–4.

[8] A. Sadeh and C. Acebo, "The role of actigraphy in sleep medicine," *Sleep Medicine Reviews*, vol. 6, no. 2, pp. 113–124, 2002.

[9] J. Liu, M. Huang, W. Xu, X. Zhang, L. Stevens, N. Alshurafa, and M. Sarrafzadeh, "Breathsens: A continuous on-bed respiratory monitoring system with torso localization using an unobtrusive pressure sensing array," *IEEE J. Biomed. Health Inform.*, vol. 19, no. 5, pp. 1682–1688, Sep. 2015.

[10] J. J. Liu, M.-C. Huang, W. Xu, and M. Sarrafzadeh, "Bodyparts localization for pressure ulcer prevention," in *Proc. 36th Annu. Conf. IEEE Eng. Med. Biol. Soc.*, Chicago, IL, USA, Aug. 2014, pp. 1–4.

[11] J. J. Liu, M.-C. Huang, W. Xu, N. Alshurafa, and M. Sarrafzadeh, "On-bed monitoring for range of motion exercises with a pressure sensitive bedsheet," in *Proc. IEEE Conf. Implantable Wearable Body Sensor Netw.*, London, U.K., May 2013, pp. 1–6.

[12] E. Hoque, R. F. Dickerson, and J. A. Stankovic, "Monitoring body positions and movements during sleep using wisps," in *Proc. ACM Wireless Health*, 2010, pp. 44–53.

[13] M. Howell Jones, R. Goubran, and F. Knoefel, "Identifying movement onset times for a bed-based pressure sensor array," in *Proc. IEEE Int. Workshop Med. Meas. Appl.*, 2006, pp. 111–114.

[14] N. Foubert, A. M. McKee, R. A. Goubran, and F. Knoefel, "Lying and sitting posture recognition and transition detection using a pressure sensor array," in *Proc. IEEE Int. Symp. Med. Meas. Appl.*, 2012, pp. 1–6.

[15] V. Verhaert, B. Haex, T. De Wilde, D. Berckmans, M. Vandekerckhove, J. Verbraecken, and J. V. Sloten, "Unobtrusive assessment of motor patterns during sleep based on mattress indentation measurements," *IEEE Trans. Inf. Technol. Biomed.*, vol. 15, no. 5, pp. 787–794, 2011.

[16] J. J. Liu, W. Xu, M.-C. Huang, N. Alshurafa, M. Sarrafzadeh, N. Raut, and B. Yadegar, "A dense pressure sensitive bedsheet design for unobtrusive sleep posture monitoring," in *Proc. IEEE Int. Conf. Pervasive Computing Commun.*, San Diego, CA, USA, Mar. 2013, pp. 207–215.

[17] S. Ostadabbas, M. Baran Pouyan, M. Nourani, and N. Kehtarnavaz, "In-bed posture classification and limb identification," in *Proc. IEEE Biomed. Circuits Syst. Conf.*, 2014, pp. 133–136.

[18] X. Shu and X.-J. Wu, "A novel contour descriptor for 2d shape matching and its application to image retrieval," *Image Vis. Comput.*, vol. 29, no. 4, pp. 286–294, 2011.

[19] Z. Ren, J. Yuan, and Z. Zhang, "Robust hand gesture recognition based on finger-earth mover's distance with a commodity depth camera," in *Proc. 19th ACM Int. Conf. Multimedia*, 2011, pp. 1093–1096.

[20] H. Ding and J. Xu, "Finding median point-set using earth mover's distance," in *Proc. 28th AAAI Conf. Artificial Intelligence*, 2014, pp. 1781–1787.

[21] K. Grauman and T. Darrell, "Fast contour matching using approximate earth mover.s distance," in *Proc. IEEE Comput. Society Conf. Comput. Vision Pattern Recognit.*, 2004, vol. 1, p. I–220.

[22] S. Cohen and L. Guibas, "The Earth Mover's Distance: Lower Bounds and Invariance Under Translation," DTIC Document, 1997, Tech. Rep.

[23] Y. Rubner, C. Tomasi, and L. J. Guibas, "The earth mover's distance as a metric for image retrieval," *Int. J. Comput. Vis.*, vol. 40, no. 2, pp. 99–121, 2000.

[24] X. Wan, "A novel document similarity measure based on earth mover's distance," *Inf. Sci.*, vol. 177, no. 18, pp. 3718–3730, 2007.

[25] N. D. Cornea, M. F. Demirci, D. Silver, A. Shokoufandeh, S. J. Dickinson, and P. B. Kantor, "3d object retrieval using many-to-many matching of curve skeletons," in *Proc. Int. Conf. Shape Modeling Appl.*, 2005, pp. 366–371.

[26] S. Boyd and L. Vandenberghe, *Convex Optimization*. Cambridge, U.K.: Cambridge Univ. Press, 2004.

[27] O. Pele and M. Werman, "Fast and robust earth mover's distances," in *Proc. IEEE 12th Int. Conf. Comput. Vision*, 2009, pp. 460–467.

[28] P. J. Huber *et al.*, "Robust estimation of a location parameter," *Ann. Math. Stat.*, vol. 35, no. 1, pp. 73–101, 1964.

[29] J. J. Liu, W. Xu, M.-C. Huang, N. Alshurafa, M. Sarrafzadeh, N. Raut, and B. Yadegar, "Sleep posture analysis using a dense pressure sensitive bedsheet," *Pervasive Mobile Comput.*, vol. 10, pp. 34–50, 2014.

[30] W. Xu, M.-C. Huang, N. Amini, L. He, and M. Sarrafzadeh, "ecushion: A textile pressure sensor array design and calibration for sitting posture analysis," *IEEE Sensors J.*, vol. 13, no. 10, pp. 3926–3934, Oct. 2013.

[31] W.-Y. Kim and Y.-S. Kim, "A region-based shape descriptor using zernike moments," *Signal Process., Image Commun.*, vol. 16, no. 1, pp. 95–102, 2000.

[32] G. Heinz, L. J. Peterson, R. W. Johnson, and C. J. Kerk, "Exploring relationships in body dimensions," *J. Stat. Educ.*, vol. 11, no. 2, pp. 2092–2101, 2003.

[33] L. Samy, M.-C. Huang, J. J. Liu, W. Xu, and M. Sarrafzadeh, "Unobtrusive sleep stage identification using a pressure-sensitive bed sheet," *IEEE Sensors J.*, vol. 14, no. 7, pp. 2092–2101, Jul. 2014.
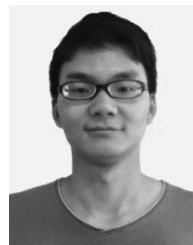
Xiaowei Xu (S'14) received the B.S. and M.S. degrees in electronic science and technology from Huazhong University of Science and Technology, Wuhan, China, in 2011 and 2014, respectively.

Currently, he is working toward the Ph.D. degree in electronic engineering in the School of Optimal and Electronic Information, Huazhong University of Science and Technology. He is a visiting student in the Department of Computer Science at the State University of New York at Buffalo, Buffalo, NY, USA. His research interests include biometrics, data mining, and embedded computing.
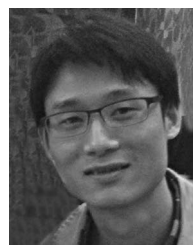
Feng Lin (S'11–M'15) received the B.S. degree from Zhejiang University, Hangzhou, China, in 2006, the M.S. degree from Shanghai University, Shanghai, China, in 2009, and the Ph.D. degree from the Department of Electrical and Computer Engineering, Tennessee Tech University, Cookeville, TN, USA, in 2015.

From 2009-2010, he worked for Alcatel-Lucent. Currently, he is a Research Scientist in the Department of Computer Science and Engineering, State University of New York (SUNY) at Buffalo, Buffalo, NY, USA. His research interests include signal processing, pattern recognition, embedded sensing, human-computer interface, wireless communications, and their applications in wireless health and biometrics.

Aosen Wang (S'15) received the B.S. degree in electrical engineering from the University of Science and Technology of China, Hefei, China, in 2011.

Currently, he is working toward the Ph.D. degree in computer science and engineering at the State University of New York (SUNY) at Buffalo, Buffalo, NY, USA. He was with Vimicro as an Algorithm and Software Engineer. His research interests include low-power computer architecture and energy-efficient machine learning.

Yu Hu (M'10) received the B.Eng. and M.Eng. degrees from the Computer Science and Technology Department, Tsinghua University, Beijing, China, in 2002 and 2005, respectively, and the Ph.D. degree from the Department of Electrical Engineering, University of California, Los Angeles, Los Angeles, CA, USA, in 2009.

From 2010 to 2012, he was an Assistant Professor in the Department of Electrical and Computer Engineering, University of Alberta, Edmonton, AB, Canada. Since 2012, he has been a Professor in the School of Optimal and Electronic Information, Huazhong University of Science and Technology, Wuhan, China. His research interests include intelligent transportation systems, connected vehicles, embedded computing, and general aspects of field-programmable gate arrays (FPGAs).

Dr. Hu was the recipient of the Outstanding Graduate Student Award from Tsinghua University in 2005, and was the corecipient of the Best Contribution Award at International Workshop of Logic and Synthesis 2008. His work was nominated for the Best Paper Award multiple times at the International Conference on Computer-Aided Design and Design Automation Conference.

Ming-Chun Huang (M'14) received the Ph.D. degree in computer science from the University of California, Los Angeles, Los Angeles, CA, USA.

Currently, he is an Assistant Professor in the Electrical Engineering and Computer Science Department, Case Western Reserve University, Cleveland, OH, USA. He has multiple years experience in pressure sensitive medical devices development, pressure map analysis, and physiological signal extraction research. He is an expert in mHealth, telemedicine, and non-invasive sensing system design. His board research interests includes the area of wearable computing, health informatics, big data analysis, human computer interaction, augmented reality, and applications of Internet of Things.

Dr. Huang received the Best Medical and Performance Application Paper Award from the IEEE Conference on Implantable and Wearable Body Sensor Networks in 2013 and the Best Demonstration Award in ACM Wireless Health Conference in 2011.

Wenyao Xu (M'13) received the Ph.D. degree from the Electrical Engineering Department, University of California, Los Angeles, Los Angeles, CA, USA, in 2013.

Currently, he is an Assistant Professor in the Computer Science and Engineering Department, State University of New York (SUNY) at Buffalo, Buffalo, NY, USA. His research foci include embedded systems, computer architecture, wireless health, low-power technologies, and their applications in biomedicine, healthcare, and security. He has five licensed U.S. and international patents, and has authored more than 70 peer-reviewed journal and conference papers.

Dr. Xu received the Best Paper Award of the IEEE Conference on Implantable and Wearable Body Sensor Networks in 2013, and the Best Demonstration Award of ACM Wireless Health Conference in 2011.